Optimization of Conical Intersections with Floating Occupation Semiempirical Configuration Interaction Wave Functions

A. Toniolo,[†] M. Ben-Nun,[†,‡] and T. J. Martínez*[,†,‡]

Department of Chemistry, University of Illinois at Urbana-Champaign, Urbana, Illinois 61801, Beckman Institute, University of Illinois at Urbana-Champaign, Urbana, Illinois 61801

Received: November 20, 2001; In Final Form: February 28, 2002

We outline a new implementation of a minimal energy conical intersection (MECI) optimization algorithm within the context of semiempirical methods. Computationally, this semiempirical conical intersection optimization method is much less demanding than ab initio CASSCF and MRCI techniques. We apply the method to several molecules and compare the geometries and energies of the resulting MECIs with ab initio CASSCF methods. The locations of the semiempirical MECIs agree very well with the ab initio predictions, but the energetics generally do not. This suggests that the semiempirical conical intersection optimization method may be useful in finding initial guess geometries for ab initio MECI searches and/or in identifying families of MECIs that may be relevant in photochemical dynamics. Indeed, in the present work, we have located many new MECIs for some of the studied molecules that were then verified and refined with ab initio electronic structure theory. The good agreement of MECIs locations further suggests that in many cases, reparametrization of semiempirical methods to reproduce both energetics and locations of MECIs may be successful.

I. Introduction

It is now widely accepted that conical intersections, i.e., true degeneracies of electronic states, play a key role in photochemical processes.[1−4] These intersections are typically not isolated points, but multidimensional seams. Nevertheless, one can ascribe special importance to the minimal energy points in the intersecting space that are often known as minimal energy conical intersections (MECIs). This is in the same spirit as the identification of the transition state as an important point in ground state reactions, and one should note that the same cautions regarding the relevance of minimal energy paths applies also to the photochemical case. In other words, usually the MECI is of importance as a representative of many energetically closely lying points in the intersecting space, just as the transition state is a representative of many possible paths over a barrier. Despite this caveat, knowing the locations and energetics of the various MECIs in a molecule provides important clues to the photochemical mechanism. Therefore it is important to be able to locate and characterize these MECI points routinely. Given the availability of analytic gradients, there are several well-tested methods for locating these intersections.[5,6] The primary obstacle to finding intersections in large molecules is the computational complexity of the electronic structure method used. A particular problem is that the quality of the electronic structure method must be quite high for even qualitatively correct results—the need to describe two degenerate states makes multireference methods necessary and typically complete active space self-consistent field (CASSCF) methods are considered the absolute minimum level of theory which is useful. An important point is that, like local minima, there may be many minimal energy conical intersections in a given molecule, located on the same or different seams. Finding all of these intersections requires initiating many searches from different initial geometries. It can be very costly to do this using CASSCF or multireference configuration interaction (MRCI) techniques, and an alternative method that is at least useful in locating fruitful approximate MECI locations would be welcome. Using a parametrized molecular-mechanics/valence-bond (MMVB) method designed for hydrocarbons, the groups of Robb and Olivucci have demonstrated the efficacy of low-level hybrid methods in locating conical intersections.[7−9] Semiempirical methods provide another computationally inexpensive alternative that can be used for this purpose.[10] However, the key question as to the accuracy of the resulting intersections and their suitability as initial guesses remains to be answered. Since most semiempirical methods have been formulated within the framework of a single-reference approach, their ability to provide a balanced treatment of multiple electronic states at widely varying molecular geometries is limited. The recently described floating occupation molecular orbital (FOMO) approach[11] circumvents this problem by determining the orbitals in a single determinant in a way that approximates a highly state-averaged CASSCF calculation. This is a generalization of the occupation-averaged SCF procedure that has been used in ab initio multiple spawning simulations of photochemistry.[4] In this paper, we describe our recent implementation of a MECI search algorithm in the FOMO-semiempirical method and compare the resulting conical intersection locations, energetics, and topographies with those obtained from ab initio methods.

II. Theory and Computational Method

It is well-known that the Born−Oppenheimer approximation fails at nuclear configurations where two electronic states are either truly or nearly degenerate. The degree to which the approximation fails is controlled by the nonadiabatic coupling

[†] Department of Chemistry.
[‡] Beckman Institute.

10.1021/jp014289y CCC: $22.00
Published on Web 04/17/2002

between states. The Hellmann−Feynmann formula for this coupling vector, $\vec{h}_{KL}$, is given by

$$\vec{h}_{KL} = \left\langle \psi_K \left| \frac{\partial}{\partial \vec{Q}} \right| \psi_L \right\rangle = \frac{\left\langle \psi_K \left| \frac{\partial H_{\mathrm{el}}}{\partial \vec{Q}} \right| \psi_L \right\rangle}{U_L - U_K} \tag{1}$$

where $|\psi\rangle$, U and H_{el} indicate the electronic wave function, energy, and Hamiltonian, respectively, and $\vec{Q}$ is the vector of internal nuclear coordinates. The existence of nuclear geometries in which two different electronic levels are degenerate is subject to the noncrossing rule: it is easy to show[12] that if $\{Q_1, ..., Q_N\}$ are the internal nuclear coordinates of a molecule, then two potential energy surfaces $U_K(\vec{Q})$ and $U_L(\vec{Q})$ with the same symmetry and spin multiplicity can coincide in a space of maximally $(N - 2)$ dimensions. Such an intersection is often called a conical intersection, and can be further classified as Jahn−Teller or Renner−Teller according to the form of the nonadiabatic coupling in the immediate neighborhood of the intersection. When two states have different spin multiplicity, and the spin−orbit coupling is neglected, the maximal dimensionality of an intersection is $(N - 1)$. In the following, we focus on conical intersections between states with the same spin multiplicity.

First, we define the nonadiabatic coupling vector $\vec{h}_{KL}$,

$$\vec{h}_{KL} = \left\langle \psi_K \left| \frac{\partial}{\partial \vec{Q}} \right| \psi_L \right\rangle \tag{2}$$

and the difference gradient vector $\vec{g}_{KL}$

$$\vec{g}_{KL} = \frac{\partial}{\partial \vec{Q}} (\langle \psi_K | H_{\mathrm{el}} | \psi_K \rangle - \langle \psi_L | H_{\mathrm{el}} | \psi_L \rangle) \tag{3}$$

Near an intersection, the degeneracy of the two potential energy surfaces is lifted most rapidly for displacements in the subspace defined by these two vectors, while along all other $(N - 2)$ coordinates the degeneracy may be preserved. A MECI can be optimized by minimizing the energy of the upper state (L) along the seam in the $(N - 2)$-dimensional subspace orthogonal to the vectors $\vec{g}_{KL}$ and $\vec{h}_{KL}$. In the following we briefly summarize the algorithm developed by Beapark et al.[5] for optimization of MECIs that we have adopted in the semiempirical context.

The vector indicating the direction that is followed during the optimization contains two terms:

$$\vec{v}_{KL} = 2(U_L - U_K)\hat{g}_{KL} + [\vec{G}_L - (\vec{G}_L \cdot \hat{g}_{KL})\hat{g}_{KL} - (\vec{G}_L \cdot \hat{h}_{KL})\hat{h}_{KL}] \tag{4a}$$

Here, $\hat{g}_{KL}$ is a unit vector along $\vec{g}_{KL}$

$$\hat{g}_{KL} = \frac{\vec{g}_{KL}}{|\vec{g}_{KL}|} \tag{4b}$$

$\vec{G}_L$ is the excited-state gradient

$$\vec{G}_L = \frac{\partial}{\partial \vec{Q}} \langle \psi_L | H_{\mathrm{el}} | \psi_L \rangle \tag{4c}$$

and $\hat{h}_{KL}$ is a unit vector along $\vec{h}_{KL}$ (orthogonal to $\vec{g}_{KL}$)

$$\hat{h}_{KL} = \frac{\vec{h}_{KL}}{|\vec{h}_{KL}|} - \left(\frac{\vec{h}_{KL}}{|\vec{h}_{KL}|} \cdot \hat{g}_{KL} \right) \hat{g}_{KL} \tag{4d}$$

The first and second terms on the rhs of eq 4a guarantee that we are looking for the hyperline of degeneracy (seam) and that we are minimizing the energy of the upper state along the $(N - 2)$-dimensional seam, respectively. Note that the first and second terms of eq 4a do not have the same physical dimensions. Therefore we cannot properly calculate a function given by the integral in the nuclear coordinate space of the vector $\vec{v}_{KL}$. However, as required in many optimization algorithms that resort to line minimization procedures, we define the "energy" function, corresponding to the "gradient" $\vec{v}_{KL}$, simply as $(U_L - U_K)^2$.

We have implemented this algorithm in a development version of the semiempirical MOPAC2000[13] program. The Broyden−Fletcher−Golfarb−Shanno (BFGS) method[14] is used for the optimization. The electronic wave functions are defined with configuration interaction (CI) using orbitals determined from the floating occupation molecular orbital SCF procedure.[11] In the FOMO procedure, the orbital occupation numbers in the energy expression can be fractional and variable, although physical constraints of course demand them to be positive semidefinite and no greater than two. The energy expression for orbital optimization comes from a statistical average of the energies of an ensemble of single-determinant wave functions. The orbital occupation numbers, which are related to the statistical weights of the single determinant wave functions included in the average, are chosen according to a Gaussian centered around the MO energy level. The population of the ith MO is distributed along the energy axis according to a Gaussian function, centered at the MO energy ϵ_i:

$$G_i(\epsilon) = \sqrt{\frac{2}{\pi\omega^2}} \mathrm{e}^{-(\epsilon - \epsilon_i)^2/(2\omega^2)} \tag{5}$$

Here the orbital energy width ω is an arbitrary parameter. At each SCF iteration, the occupation numbers and density matrix are obtained as

$$O_i = \int_{-\infty}^{\epsilon_{\mathrm{F}}} G_i(\epsilon)\, \mathrm{d}\epsilon \tag{6}$$

$$\rho_{ij} = \sum_k c_{ik} O_k c_{jk} \tag{7}$$

respectively, where c are the MO coefficients (from the previous iteration). The Fermi energy ϵ_{F} is set by imposing the sum of the occupation numbers to equal the total number of electrons, i.e., $\sum_i O_i = n_{\mathrm{elec}}$. This scheme is repeated self-consistently until convergence. In principle, all MO's take part in the summation, because a priori one cannot define an orbital as occupied or virtual. In practice, we employ the active space concept and decompose the orbital basis into closed, active, and virtual orbitals. Only the occupation numbers of the active orbitals, which are usually taken to be the same orbitals that are involved in the subsequent CI expansion, are allowed to be fractional. This technique allows a partial optimization of all the virtual orbitals included in the CI expansion so that the description of excited states is significantly improved. Moreover, the occupation numbers follow the molecular geometry, ensuring orbital degeneracy when necessary. In contrast to complete active space self-consistent field methods,[15] the FOMO approach does not require a multiconfigurational wave function ansatz to populate virtual orbitals and constitutes a very effective and fast computational technique. In all the test calculations and examples presented below, we adopted the value of 0.20 hartree for the Gaussian width of the orbital occupation. The CI wave

functions used vary according to the electronic structure of the system under study and are specified explicitly as required.

For CI wave functions, the nonadiabatic coupling vector $\vec{h}_{KL}$ required to evaluate $\vec{v}_{KL}$ is given by

$$\vec{h}_{KL} = \frac{1}{U_L - U_K}\mathbf{C}_K^{\dagger}\frac{\partial \mathbf{H}_{\mathrm{CI}}}{\partial \vec{Q}}\mathbf{C}_L + \sum_{uv}(\rho_{IJ})_{uv}\left\langle \varphi_u \middle| \frac{\partial \varphi_v}{\partial \vec{Q}} \right\rangle \quad (8)$$

The first term (the "CI term") on the rhs of eq 8 dominates the expression close to a conical intersection. It contains the CI eigenvectors (**C**), the eigenvalues of the two states (U), and the derivative of the CI Hamiltonian ($\partial \mathbf{H}_{\mathrm{CI}}/\partial \vec{Q}$). The second term (the "MO term") includes the molecular orbital mixing matrix, and the one-electron transition density matrix (ρ) whose elements in the second quantization formalism are given by

$$(\rho_{KL})_{uv} = \sum_{IJ} C_{K,I} C_{L,J} \langle \Phi_I | a_v^{\dagger} a_u | \Phi_J \rangle \quad (9)$$

where $C_{K,I}$ indicates the Ith element of the CI eigenvector of the Kth state in the basis of determinants $|\Phi_I\rangle$. Note that the sum over u and v in eq 8 involves only those orbitals correlated in the CI wave function. Moreover, with the exception of the transition density matrix, all other quantities are computed during the coupled perturbed HF procedure, which is required for the analytical gradient of CI potential energy surfaces.[16−18] The distinction between the "CI-term" and the "MO-term" is not completely clean—in fact, the CI-term implicitly depends on the orbitals through the definition of $\mathbf{H}_{\mathrm{CI}}$. Lengsfield and Yarkony have given a complete discussion of the meaning and computation of these contributions to the nonadiabatic coupling vector.[19] If the coordinate system is chosen correctly, the singular part of the nonadiabatic coupling vector can be concentrated in a single element. In an arbitrary coordinate system, the singular contribution will, of course, be distributed among all elements of the vector.[20]

As noted in eq 4a, the expression given for the "energy" function and the "gradient" vector $\vec{v}_{KL}$ are not consistent. In practice this means that optimization of a MECI requires finding a simultaneous zero of both the "gradient" and the "energy." The BFGS algorithm employs a line minimization procedure where only the "energy," which in our case is the squared energy gap, is minimized. As a result, the seam is rapidly reached although the gradient could be still large. In practice this can lead to highly distorted molecular geometries corresponding to configurations of high potential energy, making it difficult to find the MECI. Therefore, we avoid the line minimization procedure, moving the geometry along the "gradient" with a fixed step of 0.15 times that predicted by the Newton method.[14]

A further technical point related to the inconsistency of the "energy" and "gradient" regards the approximate Hessian that is constructed during the BFGS procedure. When the squared energy gap is large, the expression for the "gradient" is dominated by the energy difference gradient. However, once a seam is located, the expression for the "gradient" is dominated by the projection of the upper state energy gradient out of the $\vec{g}-\vec{h}$ plane. The corresponding Hessian matrix therefore depends on the current estimate of the $\vec{g}-\vec{h}$ plane. In principle, this implies that an updating scheme to approximate the Hessian matrix should not be used at all. However, the $\vec{g}-\vec{h}$ plane is often slowly varying once a seam has been located. A useful procedure is then to reinitialize the approximate Hessian matrix whenever the $\vec{g}-\vec{h}$ plane changes significantly. We use the dot product of the projected upper state energy gradient vectors from the current iteration and the last iteration where the Hessian matrix was reinitialized as a numerical measure of the change in the $\vec{g}-\vec{h}$ plane estimate. When this drops below a certain threshold, which we take to be 0.5, the approximate Hessian matrix is reinitialized. This procedure accelerates the convergence of the MECI optimization significantly.

TABLE 1: Semiempirical Energies (eV) Relative to the S_0 Equilibrium Geometry, for the Benzene Molecule at Three Different Geometries: Ground State and First Excited State Equilibrium, and the Minimal Energy Conical Intersections[a]

		S_0 min S_1	S_1 min S_0	S_1 min S_1	MECI[b] S_0/S_1
AM1	CASCI(6/6)	3.76	0.29	3.42	4.53
	CISD(6/6)	3.91	0.31	3.63	4.92
PM3	CASCI(6/6)	3.19	0.10	3.09	4.67
	CISD(6/6)	3.54	0.08	3.38	5.00
MNDO	CASCI(6/6)	2.57	0.08	2.49	4.25
	CISD(6/6)	2.90	0.05	2.85	4.66
MCSCF/4-31G		5.02		4.81	5.92
exp		4.9			

[a] The results are compared to ab initio[26] and experimental values.[27] [b] Figure 1.

III. Applications

The only practical way to assess the utility of semiempirical methods in locating MECIs is to compare directly with ab initio methods. In this section, we apply the FOMO semiempirical CI method with various standard parametrizations to a set of photochemically interesting molecules for which we have also located (or obtained from the existing literature) MECIs using ab initio state-averaged CASSCF wave functions. The three semiempirical parametrizations used are AM1,[21] PM3,[22] and MNDO.[23] The MOLPRO program[18] has been used to obtain the ab initio data, with basis sets and active spaces as described below. The molecular geometries of the MECIs are compared, along with energetic data, the $\vec{g}_{KL}$ and $\vec{h}_{KL}$ defining the intersection space, and the shape of the PESs in the vicinity of the MECI. The topography around MECIs is an important factor in the "funneling" character of the MECI and can strongly influence the nonadiabatic dynamics around the MECI.[1,24,25]

1. Benzene. Benzene is the paradigmatic aromatic molecule and therefore its photochemistry is of great interest. We use an active space with six electrons in six orbitals in our semiempirical MECI searches and assess the influence of the configurations included in the CI by using both CASCI and CISD. In both CI expansions, excitations are only allowed within the chosen active space. In the CASCI all possible determinants generated from excitations inside the active space are included while the CISD wave function is further restricted to include only single and double excitations within the active space from the Hartree−Fock-like reference. Our semiempirical results are compared to a previous MCSCF study of the conical intersections in benzene.[26] Table 1 shows the energies of the first two electronic states at three different optimized geometries: the equilibrium S_0 and S_1 geometries and the lowest energy conical intersection. The latter was obtained by using slightly distorted S_0 and S_1 equilibrium geometries as an initial guess, and the resulting geometry is shown in Figure 1. All three semiempirical parametrizations strongly underestimate the energy gap between S_0 and S_1, as evidenced by comparing the vertical excitation energies with either ab initio[26] or experimental results.[27] This tendency is most pronounced for the MNDO parametrization, and the best agreement, which is still quite poor, is obtained

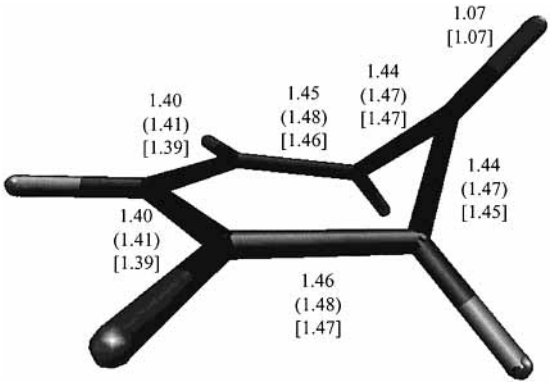

Figure 1. Final geometry of the lowest energy MECI of benzene at the AM1 CASCI(6/6) level of theory. Bond lengths are in Å, and those enclosed in parentheses and square brackets are taken from refs 26 and 40, respectively.

with the AM1 parametrization. As expected, the CISD wave function produces larger vertical excitation energies because the restricted CI expansion correlates the ground state more effectively than the excited state. Despite the poor performance of the semiempirical methods for vertical excitation energies, Table 2 shows that the equilibrium geometries on S_0 and S_1 are in excellent agreement with both the ab initio and experimental results for all three semiempirical parametrizations. Furthermore, as shown in Figure 1, the geometry of the MECI obtained with the AM1 parametrization is also in excellent agreement with previous ab initio calculations.

TABLE 2: Semiempirical Geometries for the Ground and First Excited States of the Benzene Molecule Compared with the Corresponding ab Initio and Experimental Results

		S_0		S_1	
		C−C	C−H	C−C	C−H
AM1	CASCI(6/6)	1.398	1.099	1.434	1.090
	CISD(6/6)	1.397	1.099	1.434	1.090
PM3	CASCI(6/6)	1.397	1.094	1.420	1.093
	CISD(6/6)	1.396	1.094	1.416	1.093
MNDO	CASCI(6/6)	1.415	1.089	1.435	1.087
	CISD(6/6)	1.413	1.090	1.430	1.088
MCSCF/4-31G[a]		1.39	1.07	1.43	1.07
CASSCF(6/6)/3-21G [b]		1.395	1.072	1.435	1.070
exp[c]		1.395	1.082	1.432	1.084

[a] Reference 26. [b] Reference 40. [c] References 41 and 42.

2. Ethylene. The photochemistry of ethylene has been of keen interest in our own laboratory, and we can compare the semiempirical results with accurate ab initio calculations we have previously performed.[28] For this comparison, we have chosen the ab initio results obtained at the SA-2-CASSCF-(4/7)-SDCI[29] level using the aug-cc-pVDZ basis set.[30,31] To avoid biasing the comparison toward any particular region of the potential energy surface, we have optimized the ground and the first excited state of the ethylene molecule, the ethylidene configuration, and three MECIs using AM1, PM3, and MNDO with three different wave functions: CASCI(2/2), CASCI-(6/6), and CISD(8/8), including 4, 400, and 361 determinants, respectively. In all of the nine different semiempirical techniques

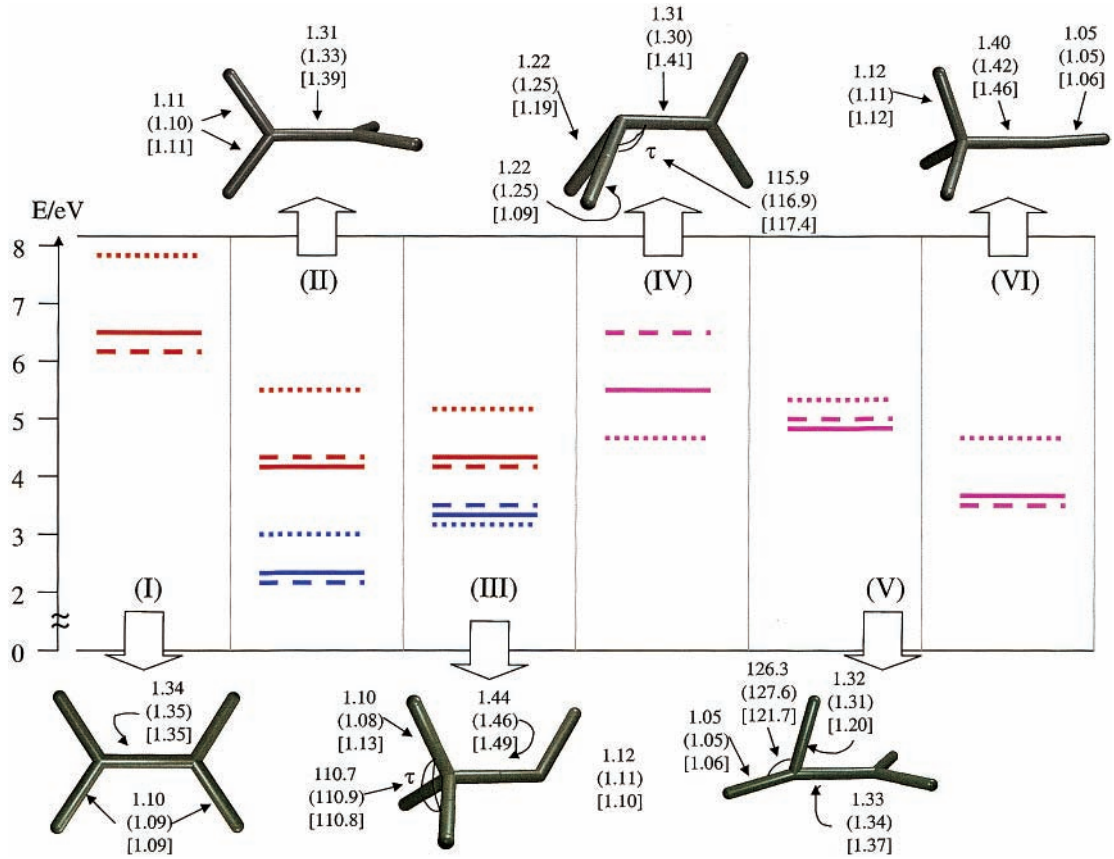

Figure 2. Ethylene ground state, first singlet excited state, and ethylidene ground-state optimized geometries (I−III, respectively) and pyramidalized, H-migration, and ethylidene conical intersections (IV−VI, respectively). The AMI-CASCI(2/2) geometrical parameters (bond lengths in Å and angles in degrees) are reported next to the corresponding structures, and the energies (eV) of the ground and first excited states are shown in the energy diagram. Here and throughout this manuscript, the zero of energy is taken to be the energy of the S_0 optimized structure at the given level of theory. Key: full line, AM1 CASCI(2/2); dashed line, MNDO CASCI(2/2); dotted line, SA-2-CASSCF(4/7). Geometrical parameters for MNDO CASCI(2/2) are enclosed in parentheses and those for the ab initio SA-2-CASSCF(4/7) wave function are enclosed in square brackets.

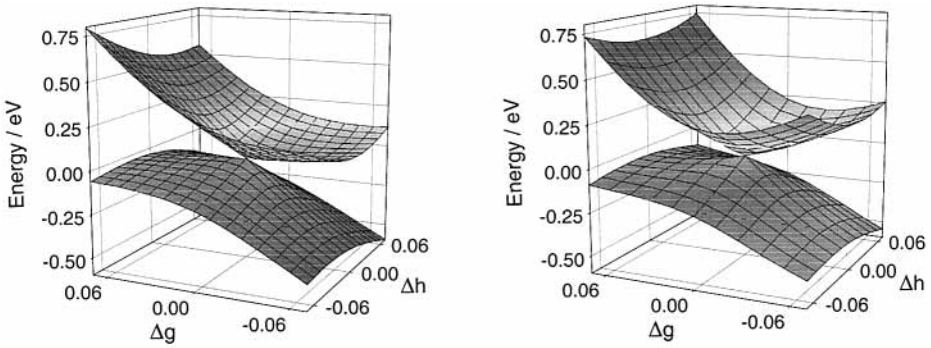

Figure 3. Ground and first singlet excited states of ethylene, computed using semiempirical AM1 CASCI(6/6) (left panel) and ab initio SA-2-CASSCF(4/7) (right panel) wave functions, as a function of displacement along the $\vec{g}$ and $\vec{h}$ vectors. All other coordinates are kept at their values at the (semiempirical, left, or ab initio, right) pyramidalized MECI (structure IV in Figure 2).

used, the structures of the optimized geometries were very similar to the ab initio ones: the ethylene ground state is planar with D_{2h} symmetry (structure I in Figure 2) and the first singlet excited state is twisted along the C−C bond with D_{2d} symmetry (structure II in Figure 2). At the semiempirical level, this twisted S_1 geometry is a true minimum, but at the ab initio level it is a saddle point, as discussed previously.[28] The ground and first excited-state optimized geometries of ethylidene have bent and linear $H_1-C_1-C_2$ structures and are shown as structures III and VI of Figure 2, respectively. At the C_{3v} linear ethylidene configuration, both S_0 and S_1 belong to the two-dimensional irreducible representation (E) and therefore the minimum of the excited state coincides with an intersection of Renner−Teller type. Two other MECIs can be identified as "pyramidalized" and "H-migration," shown as structures IV and V of Figure 2, respectively. In the pyramidalized MECI, the two methylene groups are twisted and one of the carbon atoms is pyramidalized, while in the H-migration MECI, one of the hydrogen atoms bridges between the two carbon atoms. This geometry represents an intermediate conformation between the ethylene and ethylidene configurations. The semiempirical optimized geometries are very similar to each other, despite the different parametrizations. Hence, only the AM1 results are shown in Figure 2. While we have previously located conical intersections with H-migration character, as earlier highlighted by Ohmine,[32] using ab initio methods, there is apparently no *minimal energy* intersection of this type. In contrast, the semiempirical calculations *do* find a true MECI with this character. The ab initio structure and energy shown for the H-migration intersection in structure V of Figure 2 is one of the lower-lying representatives of this class of intersections, as described in ref 28. In the case of the pyramidalized MECI shown as structure IV in Figure 2, the semiempirical methods predict a symmetric (C_s) geometry, with equal C−H bond distances involving the pyramidalized carbon atom. At the ab initio level, these bond lengths are not equal and the HCH angle is larger, reflecting some amount of H-migration character. There are significant disagreements between the semiempirical and ab initio energetics, as shown in Figure 2. Most notably, the pyramidalized MECI is an absolute minimum on the excited state in the ab initio calculations but lies above even the Franck−Condon point in the MNDO calculations. As in the case of benzene, all of the vertical excitation energies are underestimated with respect to the corresponding ab initio results. Again, the MNDO method performs most poorly overall. At the semiempirical level, the energy of the pyramidalized MECI is higher than that of the two other intersections, while at the ab initio level it is almost degenerate with the ethylidene MECI. This is partially a consequence of the different molecular geometries obtained with the semiempirical methods.

TABLE 3: Semiempirical S_0-S_1 Energy Differences (eV) for Ethylene at the ab Initio Optimized Conical Intersections[a]

		pyr ethylene MECI (IV)	H-migr ethylene intersection (V)	ethylidene MECI (VI)
AM1	CASCI(2/2)	1.41	1.24	0.00
	CASCI(6/6)	1.15	1.04	0.00
	CISD(8/8)	1.02	0.92	0.00
PM3	CASCI(2/2)	1.42	1.33	0.00
	CASCI(6/6)	1.22	1.22	0.00
	CISD(8/8)	1.07	1.08	0.00
MNDO	CASCI(2/2)	1.76	1.42	0.00
	CASCI(6/6)	1.44	1.22	0.00
	CISD(8/8)	1.35	1.08	0.00

[a] Roman numerals in parentheses refer to the corresponding geometry depicted in Figure 2. The H-migration intersection geometry chosen is simply representative, as no MECI of H-migration character could be located in the ab initio calculations.

To directly test the semiempirical description of the conical intersections, we also performed single point semiempirical calculations at the ab initio geometries of the three conical intersections. The resulting S_0-S_1 energy gaps are reported in Table 3. The CASCI(2/2) wave functions exhibit larger energy gaps as compared to larger CI expansions, implying that the CASCI(6/6) and CISD(8/8) give a description of the electronic structure which is closer to the ab initio result.

The $\vec{g}$ and $\vec{h}$ vectors as given in eqs 2 and 3 are not necessarily orthogonal, and one is really most interested in the branching plane defined by the vectors. Here and in the following, we resolve ambiguity in $\vec{g}$ and $\vec{h}$ by orthogonalizing $\vec{h}$ to $\vec{g}$ using a Gram−Schmidt procedure. After obtaining an orthogonal pair of vectors in this way for the ab initio case, the semiempirical $\vec{g}$ and $\vec{h}$ are rotated between themselves to obtain maximal agreement between the ab initio and semiempirical $\vec{g}$. The sign of the semiempirical $\vec{h}$ is then chosen to maximize overlap with the ab initio $\vec{h}$. This procedure does not change the branching plane in either the ab initio or semiempirical case and allows for a clear comparison of the molecular motions involved in lifting the degeneracy around the intersection. An alternative procedure for comparing $\vec{g}$ and $\vec{h}$ from different calculations has been proposed by Yarkony[1] and Yarkony and Matsika.[33]

Figure 3 depicts a two-dimensional cut of the ground and first excited potential energy surfaces in the vicinity of the pyramidalized MECI, as a function of the displacement along the $\vec{g}$ and $\vec{h}$ vectors (computed at the AM1 CASCI(6/6) and SA-2-CASSCF(4/7) levels of theory). Although the semiempirical and ab initio geometries of this conical intersection

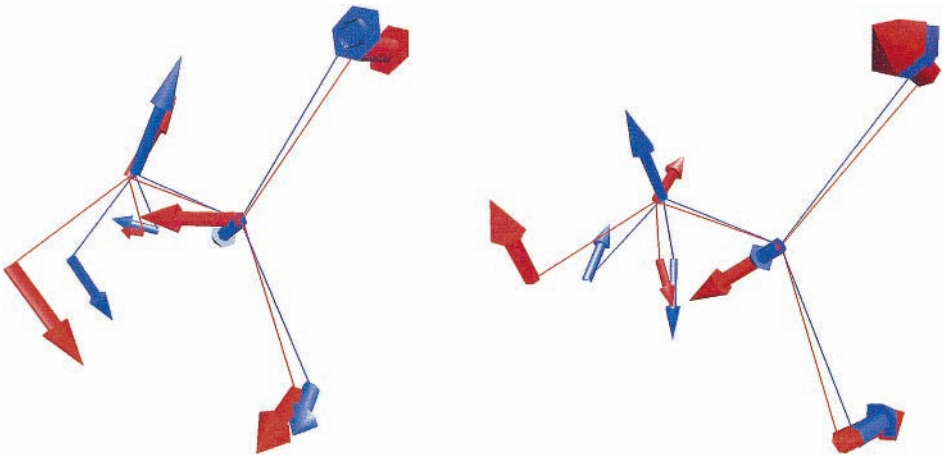

Figure 4. Comparison between semiempirical AM1 CASCI(6/6) and ab initio SA-2-CASSCF(4/7) $\vec{g}$(left panel) and $\vec{h}$ (right panel) vectors at the pyramidalized MECI of ethylene (structure IV in Figure 2). In both panels, the semiempirical results (molecular geometry and $\vec{g}$ or $\vec{h}$ vectors) are denoted in blue and the ab initio results (molecular geometry and $\vec{g}$ or $\vec{h}$ vectors) are denoted in red.

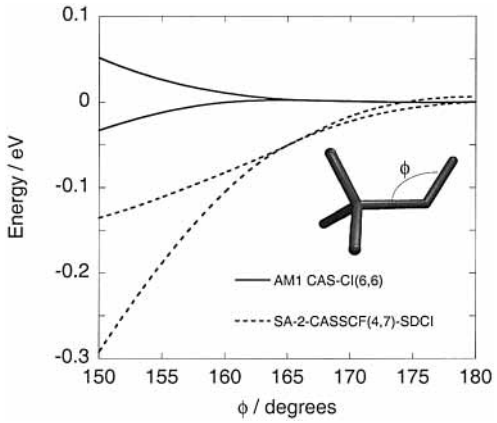

Figure 5. Semiempirical (dashed line) and ab initio (solid line) energies of the ground and first singlet excited states of ethylidene as a function of the H−C−CH_3 angle. All other geometrical parameters are held fixed at the values found for the AM1 CASCI(6/6) or ab initio SA-2-CASSCF(4/7) ethylidene MECI (structure VI in Figure 2.)

differ considerably (see Figure 2), the shape of the potential energy surfaces in the vicinity of the conical intersection is very similar. The similarity of the PESs along $\vec{g}$ and $\vec{h}$ suggests that the vectors themselves may also be quite similar. In Figure 4 we compare the ab initio and semiempirical $\vec{g}$ and $\vec{h}$ vectors. The overlap between the two gradient difference vectors is 0.84 and between the two nonadiabatic coupling vectors it is 0.54. These comparisons show that the qualitative characteristics of this MECI are predicted correctly by the AM1 method.

In the case of the linear ethylidene intersection, this comparison cannot be made. Since the two states belong to two components of the same two-dimensional irreducible representation, the vector is identically zero at this geometry. However, one can compare the shape of the PESs along the bend angle. As shown in Figure 5, the semiempirical and ab initio methods predict the same Renner−Teller behavior of this MECI (as a function of the bend angle). In this figure, we plot the energy, computed at ab initio and semiempirical levels of theory, of the first two electronic states as a function of the CCH bending angle, keeping all other internal coordinates fixed at their values for the linear C_{3v} ethylidene molecule optimized at the respective level of theory. Strictly speaking, these cuts of the potential energy surface do not include the fully optimized MECI for either level of theory, although they come very close. One difference between the ab initio and semiempirical results here is the CCH angle—for the fully optimized MECI, $\angle CCH_{\text{ab initio}} = 156.7°$ compared to $\angle CCH_{\text{semiempirical}} = 180°$.

3. Green Fluorescent Protein Chromophore. The most promising field of application for semiempirical methods is the study of large molecules, where high quality ab initio results cannot be obtained. In this section we compare semiempirical and ab initio calculations for the green fluorescent protein (*p*-hydroxybenzylidene)imidazolidinone chromophore, hereafter denoted as the GFP chromophore. We only consider the neutral form of the chromophore in the following, which is widely presumed to be the absorbing species. However, there remains some controversy on this point.[34] Experiments have established that fluorescence arises from a different protonation state of the chromophore,[35] which is almost certainly anionic. We do not consider any alternative protonation states here, which would only distract from our main goal. Our characterization of the photochemistry and photophysics in all the relevant ionic forms of the GFP chromophore will be presented in a future publication.

We chose two different types of wave functions: CASCI(6/6) and CISD(8/8), as previously described. The ab initio results for comparison have been obtained with SA-2-CASSCF(2/2) wave functions within the 6-31G basis set,[36] recently performed in our laboratory.[37] We optimized the ground and first singlet excited state geometries (Figure 6a,b, respectively) and three different MECIs. These MECIs are qualitatively quite different: the first one, shown in Figure 6c, maintains the planar structure of the ground state with a significant stretching of the phenolic O−H bond; the second one, shown in Figure 6d, involves intramolecular proton transfer from the phenolic ring to the imidazolidinone ring; and the last one, shown in Figure 6e, involves pronounced pyramidalization of a carbon atom in the imidizalidinone ring. Table 4 compares the semiempirical and ab initio results. As in the previous examples, all the energies are quoted relative to the energy of the optimized ground state. The AM1 and PM3 results are quite similar, the only exception being the pyramidalized conical intersection at the AM1 CASCI(6/6) level, which is unexpectedly high with respect to all the other methods. Again the MNDO method gives the poorest description of the system when compared to ab initio results. In particular, it is unable to reproduce the flat geometry of the optimized ground state. The relative energies of the three conical intersections show the same behavior with the lowest energy being the pyramidalized one, shown in Figure 6e. The

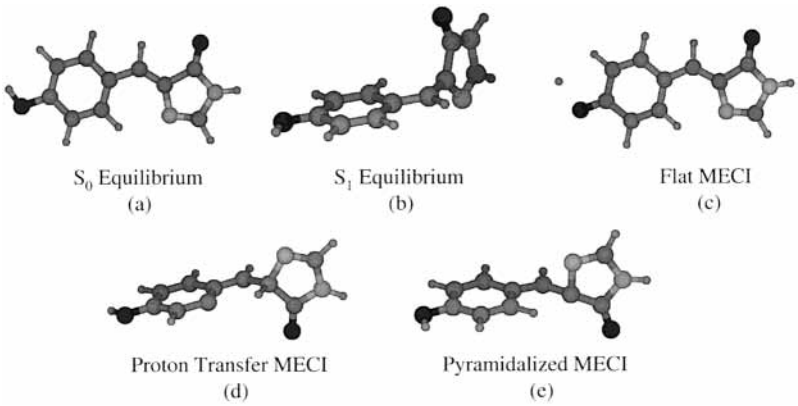

Figure 6. GFP chromophore ground (a) and first singlet excited state (b) optimized geometries. Panels (c), (d) and (e) depict the flat, proton transfer and pyramidalized MECIs, respectively.

TABLE 4: Energies (eV) of the Two Lowest Singlet States of the GFP Chromophore at Their Equilibrium Geometries and at the Three MECIs Shown in Figure 6[a]

		S_0 min (a) S_1	S_1 min (b) S_0	S_1 min (b) S_1	flat MECI (c) S_0/S_1	H^+-transfer MECI (d) S_0/S_1	pyr MECI (e) S_0/S_1
AM1	CASCI(6/6)	3.56	1.57	2.83	4.52	3.91	3.96
	CISD(8/8)	3.83	1.84	2.63	4.71	3.84	3.54
PM3	CASCI(6/6)	3.51	1.51	2.63	4.27	3.90	3.35
	CISD(8/8)	3.75	1.78	2.54	4.48	3.67	3.10
MNDO	CASCI(6/6)	3.84	1.38	2.78	5.14	4.59	3.72
	CISD(8/8)	4.14	1.66	2.57	5.32	4.19	3.33
ab initio		5.04	2.68	3.32	5.19	4.56	3.62

[a] Semiempirical and ab initio SA-2-CASSCF(2/2) results are shown. Letters enclosed in parentheses refer to the corresponding geometry depicted in Figure 6.

TABLE 5: Semiempirical S_0-S_1 Energy Differences (eV) for the GFP Chromophore at the ab Initio Optimized MECIs[a]

		flat MECI (c)	H^+-transfer MECI (d)	pyr MECI (e)
AM1	CASCI(6/6)	0.50	0.69	0.91
	CISD(8/8)	0.01	0.42	0.51
PM3	CASCI(6/6)	0.55	0.83	0.82
	CISD(8/8)	0.20	0.43	0.48
MNDO	CASCI(6/6)	1.20	1.00	1.07
	CISD(8/8)	0.36	0.65	0.51

[a] Letters enclosed in parentheses refer to the corresponding geometry depicted in Figure 6.

use of the CISD(8/8) instead of the CASCI(6/6) wave function gives a slightly different description of the electronic structure of the molecule. At the CISD level of calculation, the energies of the excited state are lower at the twisted geometries, while they are higher at the flat ones.

To further compare the semiempirical and ab initio results, we have performed semiempirical single point calculations at the ab initio MECI geometries. As shown in Table 5, the resulting S_0-S_1 energy gaps are quite large. However, as shown in Figure 7, the semiempirical and ab initio optimized geometries differ appreciably only in case of the pyramidalized MECI. Therefore, the relevant energy gaps could be due to a strongly peaked character of the MECIs.[1,24] The AM1 CISD(8/8) wave function gives rise to the smallest energy gaps and therefore the most similar description to the ab initio method for the potential energy surfaces in the vicinity of this MECI.

In Figure 7 we also compare the nonadiabatic coupling vector, and the gradient difference vector $\vec{g}$, of the AM1 CISD(8/8) and ab initio methods, at the three conical intersections of GFP. Clearly, the $\vec{g}$ and $\vec{h}$ vectors are very similar: The overlap between the semiempirical and the corresponding ab initio vectors lies between 0.65 and 0.95, while the overlap defined as

$$O = \frac{1}{2}(\vec{g}_{SE} + \vec{h}_{SE})\cdot(\vec{g}_{AI} + \vec{h}_{AI}) \qquad (10)$$

is always greater than 0.94. The formula in eq 10 provides an appropriate comparison of the branching planes in the case where $\vec{g}$ and $\vec{h}$ for the ab initio and semiempirical methods have been put into maximum coincidence, as described before.

4. Retinal Protonated Schiff Base. An example of general interest in the field of polyene photochemistry is retinal protonated Schiff base (RPSB), the chromophore in the rhodopsin family of proteins, which serves as a paradigm for understanding the biological mechanism of converting light to mechanical energy. For a large model of the RPSB chromophore, neglecting only the β-ionone ring, we have compared the semiempirical results obtained using a CISDT(10/8) wave function (1236 determinants) with those obtained using an ab initio SA-2-CASSCF(10/10)/6-31G* wave function. Both methods include all 10 π electrons in the active space. In Table 6, we compare the vertical excitation energies, computed at the respective optimized ground state geometries shown in Figure 8a. All the semiempirical methods predict much lower vertical transition energies than the CASSCF one. This is certainly partially due to the deficiencies of the CASSCF wave function that neglects the dynamical correlation energy. However, EOM-CCSD calculations[38] done in our laboratory (not shown) suggest that the semiempirical methods overcorrect, so that the true vertical excitation energy is bracketed by the semiempirical and ab initio results. Optimization of the first singlet excited-state converged to a local minimum with a twisted $C_{13}-C_{14}$ bond

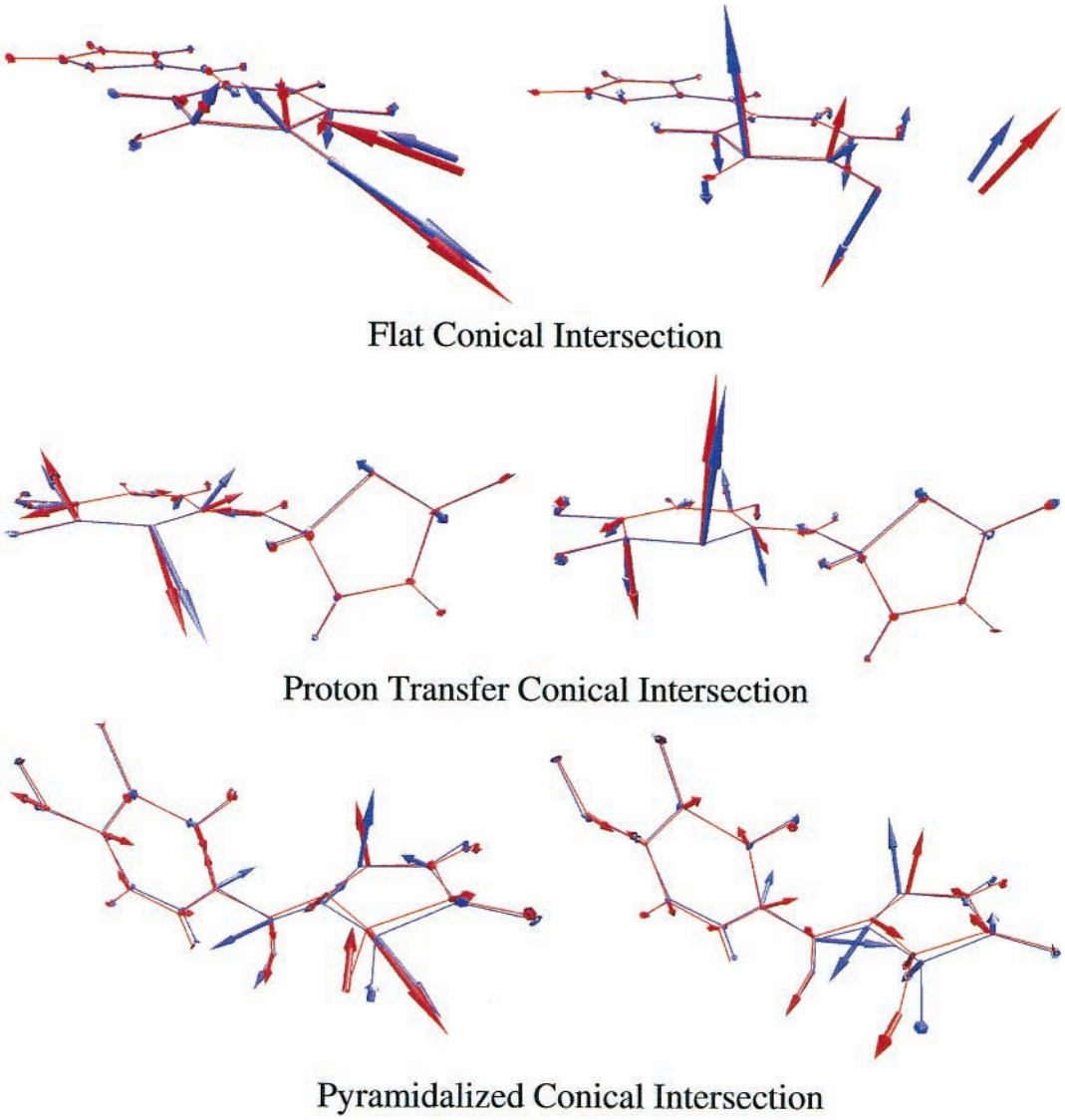

Figure 7. Comparison between semiempirical AM1 CISD(8/8) and ab initio SA-2-CASSCF(2/2)/6-31G $\vec{g}$ (left panels) and $\vec{h}$ (right panels) vectors at the three MECIs of the GFP chromophore depicted in Figure 6. In both panels, the semiempirical results (molecular geometry and $\vec{g}$ or $\vec{h}$ vectors) are denoted in blue and the ab initio results (molecular geometry and $\vec{g}$ or $\vec{h}$ vectors) are denoted in red.

TABLE 6: Semiempirical and ab Initio S_0-S_1 Energies (eV) for Retinal Protonated Schiff Base[a]

		S_0 min (a) S_1	S_1 min $C_{13}-C_{14}$ twisted (b) S_0	S_1 min $C_{13}-C_{14}$ twisted (b) S_1	$C_{11}-C_{12}$ twisted MECI (c) S_0/S_1	N-pyr MECI (d) S_0/S_1	$C_{13}-C_{14}$ twisted MECI (e) S_0/S_1	C_9-C_{10} twisted MECI (f) S_0/S_1
AM1	CISDT(10/8)	2.22	0.90	1.79	1.31	2.11	2.24	1.63
PM3	CISDT(10/8)	2.18	0.86	1.55	1.33	2.04	2.00	1.65
MNDO	CISDT(10/8)	1.94	0.84	1.34	1.06	1.56	1.77	1.27
ab initio	SA-2-CASSCF(10/10)	3.51	2.17	2.32	2.30	3.63	2.35	*b*

[a] All energies refer to the ground state equilibrium energy, and the last four columns report only the S_1 energy because the two states are degenerate. Letters enclosed in parentheses refer to the corresponding geometry depicted in Figure 8. [b] At the ab initio level of calculation we did not locate a MECI involving torsion around the $C_9=C_{10}$ bond. The ground and excited state ab initio energies at the semiempirical MECI geometries are 3.14 and 3.38 eV (respectively). The relatively small energy gap implies that the semiempirical MECI geometry is close to a seam of conical intersections and an ab initio MECI search that starts from it converges to the MECI associated with torsion around the $C_{11}=C_{12}$ bond.

shown in Figure 8b, and to an absolute minimum with a twisted central $C_{11}-C_{12}$ bond shown in Figure 8c. The ab initio calculations find the $C_{11}=C_{12}$ and $C_{13}=C_{14}$ MECIs to be essentially degenerate, but the semiempirical methods find a significant energetic difference between the MECIs—in the AM1 case, this is so pronounced that the $C_{13}=C_{14}$ MECI lies above the Franck−Condon point. However, the semiempirical and ab initio methods do agree that there is no true minimum for twisting around the $C_{11}=C_{12}$ bond—the lowest energy structure is a conical intersection. As shown in Table 6, the semiempirical methods find a higher S_0-S_1 energy gap at the optimized excited-state $C_{13}-C_{14}$ twisted geometry, and they place the corresponding MECI, Figure 8e, about 0.45 eV above the energy of the S_1 local minimum, Figure 8b. Also the relative energies of the $C_{11}-C_{12}$ and $C_{13}-C_{14}$ twisted MECIs are different at the semiempirical and ab initio levels of theory. They are almost

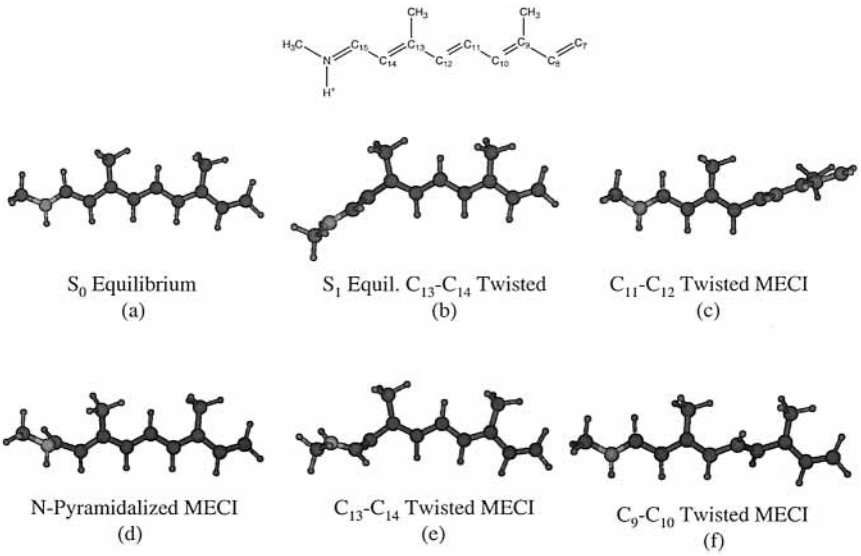

Figure 8. Model retinal protonated Schiff base ground (a) and first singlet excited-state $C_{13}-C_{14}$ twisted (b) optimized geometries. Also depicted are the $C_{11}-C_{12}$ twisted (c), N-pyramidalized (d), $C_{13}-C_{14}$ twisted (e) and C_9-C_{10} twisted (f) MECIs.

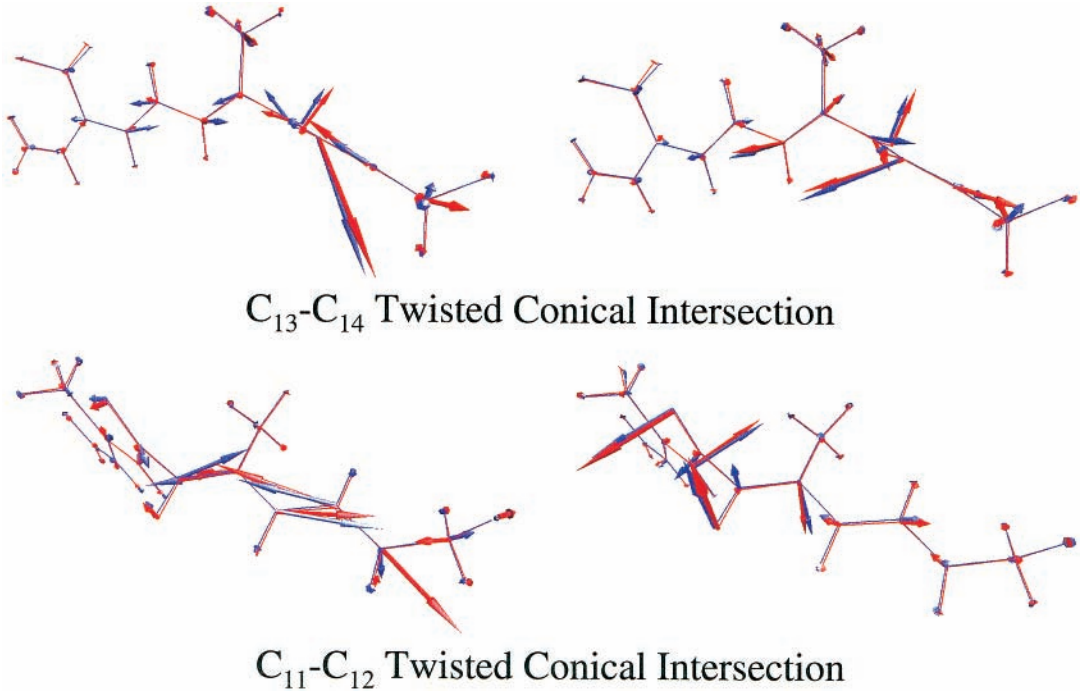

Figure 9. Comparison between semiempirical PM3 CISDT(10/8) and ab initio SA-2- CASSCF(10/10)/6-31G* $\vec{g}$ (left panels) and $\vec{h}$ (right panels) vectors at the $C_{13}-C_{14}$ twisted (structure depicted in Figure 8e) and $C_{11}-C_{12}$ twisted (structure depicted in Figure 8c) MECIs of a model retinal protonated Schiff base. In both panels the semiempirical results (molecular geometry and $\vec{g}$ or $\vec{h}$ vectors) are denoted in blue and the ab initio results (molecular geometry and $\vec{g}$ or $\vec{h}$ vectors) are denoted in red.

degenerate at the ab initio level, while the energy of the $C_{11}-C_{12}$ MECI is lower by 0.7−1.0 eV than that of the $C_{13}-C_{14}$ MECI at the semiempirical level.

Starting from different guess geometries, we found two additional MECIs at the semiempirical level: one is twisted along the $C_{13}-C_{14}$ bond with a pyramidalized nitrogen atom ("N-pyramidalized"), as shown in Figure 8d, and the other involves twisting of the C_9-C_{10} bond and the two adjacent bonds ("C_9-C_{10} twisted"), as shown in Figure 8f. Both are lower in energy than the $C_{13}-C_{14}$ twisted MECI shown in Figure 8e. A search for these MECIs at the ab initio level did find an analogous "N-pyramidalized" MECI. However, it is quite high in energy at the ab initio level. While we did not find a MECI starting from the semiempirical "C_9-C_{10} twisted" MECI, this does not preclude the existence of a MECI of similar character—indeed, the ab initio S_0-S_1 energy gap at the semiempirical C_9-C_{10} twisted MECI geometry is relatively small (0.24 eV), indicating that there may be an intersection seam nearby. However, the ab initio energy is again quite high compared to that predicted by the semiempirical method.

In Figure 9 we report, with different colors, the optimized geometries at the $C_{13}-C_{14}$ and $C_{11}-C_{12}$ conical intersections, obtained at the ab initio and PM3 levels of theory. Their superposition is almost perfect, confirming that the semiempirical method constitutes a very efficient strategy for fast location of MECIs in large molecules or, at least, for initial guesses that can be used in ab initio optimizations. The small differences in the geometries at these two MECIs can be

TABLE 7: Semiempirical S_0-S_1 Energy Differences (eV) for the Model Retinal Protonated Schiff Base at the ab Initio Optimized MECIs[a]

		$C_{13}-C_{14}$ twisted MECI (e)	$C_{11}-C_{12}$ twisted MECI (c)
AM1	CISDT(10/8)	0.97	0.19
PM3	CISDT(10/8)	0.57	0.01
MNDO	CISDT(10/8)	0.71	0.10

[a] Letters enclosed in parentheses refer to the corresponding geometry depicted in Figure 8.

discerned by performing single point semiempirical calculations at the ab initio geometries. As shown in Table 7, the S_0-S_1 energy gaps lie between 0.6 and 1.0 eV and below 0.2 eV for the $C_{13}-C_{14}$ and the $C_{11}-C_{12}$ MECIs, respectively.

Direct comparison of the $\vec{g}$ and $\vec{h}$ vectors, shown in Figure 9, demonstrates again that the semiempirical method (PM3 in this case) captures much of the qualitative behavior of the potential energy surfaces around the MECIs as described by the more trustworthy SA-2-CASSCF(10/10) wave function. The overlap between the $\vec{g}$ vectors is 0.95 and 0.94, and between the $\vec{h}$ vectors it is 0.76 and 0.91, for the $C_{11}-C_{12}$ and $C_{13}-C_{14}$ MECIs, respectively.

IV. Conclusions

In this paper we presented a new implementation of Bearpark's et al.[5] minimal energy conical intersection search algorithm within the context of semiempirical methods. Computationally, the semiempirical conical intersection search algorithm is much less demanding than ab initio CASSCF and MRCI techniques and it is therefore very attractive. In the present work we used several photochemically interesting molecules (benzene, ethylene, GFP chromophore, and retinal protonated Schiff base) to assess the accuracy of three semiempirical methods (AM1, PM3, and MNDO) by comparison with ab initio CASSCF results.

The MECI search algorithm was implemented in a development version of the semiempirical MOPAC2000[13] program using a configuration interaction electronic wave function with orbitals determined from the floating occupation molecular orbital SCF procedure introduced by Granucci and Toniolo.[11] The FOMO procedure provides a fast and effective means to approximate the orbitals that would be obtained in a state-averaged CASSCF method, without using an explicit multiconfiguration wave function ansatz. In this procedure the orbital occupation numbers in the energy expression are allowed to be fractional and partial optimization of all the virtual orbitals within a chosen active space is allowed. This significantly improves the description of excited states, and because the occupation numbers follow the molecular geometry, orbital degeneracy is ensured, when necessary.

To assess the accuracy and utility of the semiempirical methods in locating MECIs, we have compared the geometries, energies and local topographies (two-dimensional cuts of the PES along the $\vec{g}$ and $\vec{h}$ vectors) of the semiempirical MECIs to the ones located using ab initio state averaged CASSCF methods. When experimental data were available, we have also made appropriate comparisons, e.g., equilibrium geometries and vertical excitation energies. Of the three semiempirical parametrizations that we tested, we found that the AM1 and PM3 results are of similar accuracy while the accuracy of the MNDO results is significantly lower, where high accuracy implies agreement with ab initio and/or experimental results. The locations of the AM1 and PM3 MECIs and their local topographies (i.e., both the $\vec{g}-\vec{h}$ planes and the individual projections of the $\vec{g}$ and $\vec{h}$ vectors) generally agree very well with the ab initio predictions but the same is not true for the relative energies. In many instances we found that the semiempirical methods fail to predict the correct relative energies, even qualitatively. This is not too surprising since these methods were typically parametrized to reproduce ground state atomic and molecular properties and have not been reparametrized in the context of fractional occupation methods. Nevertheless, we find the results promising in two contexts. First, semiempirical conical intersection search methods can be very effective in finding initial guess geometries for the (computationally much more intensive) ab initio MECI searches, or simply in enumerating the coordinates that play a significant role in different families of MECIs. Indeed, in this work we have located many new MECIs for two of the studied molecules (GFP chromophore and retinal protonated Schiff base) using semiempirical conical intersection search methods. These intersections were then verified and refined with ab initio electronic structure methods. Although we have used state-averaged CASSCF for the ab initio method in this work, one could also use more accurate second-order CI methods[1] that include dynamic electron correlation given molecules small enough to make this computationally tractable. Second, the good agreement of MECIs geometries suggests that in many cases reparametrization of semiempirical methods to reproduce both the energetics and location of MECIs may be successful without too much effort. In our lab this reparametrization is currently being pursued for several molecules with favorable preliminary results.

Acknowledgment. We thank Prof. M. A. Robb for helpful discussions. Financial support for this work was provided by the National Institutes of Health (PHS-5-P41-RR05969) and the National Science Foundation (CHE-97-33403 and DMR-99-76550). T.J.M. is the grateful recipient of CAREER, Beckman Young Investigator, Packard Fellow, Sloan Fellow and Dreyfus Teacher-Scholar awards from NSF, and the Beckman, Packard, Sloan, and Dreyfus Foundations, respectively. VMD[39] was used to generate some of the figures.

References and Notes

(1) Yarkony, D. R. *J. Phys. Chem. A* **2001**, *105*, 6277.
(2) Klessinger, M.; Michl, J. *Excited States and Photochemistry of Organic Molecules*; VCH Publishers: New York, 1995.
(3) Garavelli, M.; Bernardi, F.; Olivucci, M.; Vreven, T.; Klein, S.; Celani, P.; Robb, M. A. *Faraday Discuss.* **1998**, *110*.
(4) Ben-Nun, M.; Quenneville, J.; Martínez, T. J. *J. Phys. Chem. A* **2000**, *104*, 5161.
(5) Bearpark, M. J.; Robb, M. A.; Schlegel, H. B. *Chem. Phys. Lett.* **1994**, *223*, 269.
(6) Yarkony, D. R. Electronic Structure Aspects of Nonadiabatic Processes in Polyatomic Systems. In *Modern Electronic Structure Theory*; Yarkony, D. R., Ed.; World Scientific: Singapore, 1995; p 642.
(7) Beapark, M. J.; Bernardi, F.; Clifford, S.; Olivucci, M.; Robb, M. A.; Vreven, T. *Mol. Phys.* **1996**, *89*, 37.
(8) Beapark, M. J.; Bernardi, F.; Olivucci, M.; Robb, M. A. *Int. J. Quantum Chem.* **1996**, *60*, 505.
(9) Beapark, M. J.; Celani, P.; Jolibois, F.; Olivucci, M.; Robb, M. A.; Bernardi, F. *Mol. Phys.* **1999**, *96*, 645.
(10) Izzo, R.; Klessinger, M. *J. Comput. Chem.* **2000**, *21*, 52.
(11) Granucci, G.; Toniolo, A. *Chem. Phys. Lett.* **2000**, *325*, 79.
(12) Landau, L. D.; Lifschitz, E. M. *Quantum Mechanics*; Pergamon: New York, 1965.
(13) Stewart, J. J. P. MOPAC2000; Fujitsu Limited: Tokyo, Japan, 1999.
(14) Press: W. H.; Teukolsky, S. A.; Vetterling, W. T.; Flannery, B. P. *Numerical Recipes*; Cambridge University Press: Cambridge, 1992.
(15) Roos, B. O. The Complete Active Space Self-Consistent Field Method and its Applications in Electronic Structure Calcculations. In *Advances in Chemical Physics: Ab Initio Methods in Quantum Chemistry II*; Lawley, K. P., Ed.; John Wiley and Sons Ltd.: New York, 1987; p 399.
(16) Gerratt, J.; Mills, I. M. *J. Chem. Phys.* **1964**, *49*, 1719.

(17) Yamaguchi, Y.; Osamura, Y.; Goddard, J. D.; Schaefer, H. F. *A New Dimension to Quantum Chemistry: Analytic Derivative Methods in Ab Initio Electronic Structure Theory*; Oxford University Press: Oxford, U.K., 1994.

(18) Werner, H.-J.; Knowles, P. J.; Almlöf, J.; Amos, R. D.; Berning, A.; Cooper, D. L.; Deegan, M. J. O.; Dobbyn, A. J.; Eckert, F.; Elbert, S. T.; Hampel, C.; Lindh, R.; Lloyd, A. W.; Meyer, W.; Nicklass, A.; Peterson, K.; Pitzer, R.; Stone, A. J.; Taylor, P. R.; Mura, M. E.; Pulay, P.; Schütz, M.; Stoll, H.; Thorsteinsson, T. MOLPRO 98.1, 1998.

(19) Lengsfield, B. H.; Yarkony, D. R. Nonadiabatic Interactions between Potential Energy Surfaces: Theory and Applications. In *State-Selected and State to State Ion−Molecule Reaction Dynamics*; Baer, M., Ng, C.-Y., Eds.; John Wiley and Sons: New York, 1992; p 1.

(20) Matsika, S.; Yarkony, D. R. *J. Phys. Chem. A* **2002**, *106*, 2591.

(21) Dewar, M. J. S. *J. Am. Chem. Soc.* **1985**, *107*, 3902.

(22) Dewar, M. J. S. *J. Comput. Chem.* **1989**, *10*, 209.

(23) Dewar, M. J. S.; Thiel, W. *J. Am. Chem. Soc.* **1977**, *99*, 4899.

(24) Atchity, G. J.; Xantheas, S. S.; Ruedenberg, K. *J. Chem. Phys.* **1991**, *95*, 1862.

(25) Yarkony, D. R. *J. Chem. Phys.* **2001**, *114*, 2601.

(26) Palmer, L. J.; Ragazos, I. N.; Bernardi, F.; Olivucci, M.; Robb, M. A. *J. Am. Chem. Soc.* **1993**, *115*, 6732.

(27) Bolovinos, A.; Tskeris, P.; Philis, J.; Pantos, E.; Andritsopulos, G. *J. Mol. Spectrosc.* **1984**, *103*, 240.

(28) Ben-Nun, M.; Martínez, T. J. *Chem. Phys.* **2000**, *259*, 237.

(29) SA-*x*-CASSCF(*m*,*n*)-SDCI denotes a multireference single and double excitation configuration interaction wave function using orbitals derived from a CASSCF calculation with *m* electrons in *n* orbitals averaged over the lowest *x* electronic states without symmetry constraints.

(30) Dunning, T. H. J. *J. Chem. Phys.* **1989**, *90*, 1007.

(31) Kendall, R. A.; Dunning, T. H., Jr.; Harrison, R. J. *J. Chem. Phys.* **1992**, *96*, 6796.

(32) Ohmine, I. *J. Chem. Phys.* **1985**, *83*, 2348.

(33) Matsika, S.; Yarkony, D. R. *J. Chem. Phys.* **2001**, *115*, 5066.

(34) Voityuk, A. V.; Michel-Beyerle, M.-E.; Rosch, N. *Chem. Phys. Lett.* **1998**, *296*, 269.

(35) Chattoraj, M.; King, B. A.; Bublitz, G. U.; Boxer, S. G. *Proc. Natl. Acad. Sci. U.S.A.* **1996**, *93*, 8362.

(36) Hehre, W. J.; Ditchfield, R.; Pople, J. A. *J. Chem. Phys.* **1972**, *56*, 2257.

(37) Seth Olsen, Leslie Manohar, and Todd J. Martinez, manuscript in preparation.

(38) Stanton, J. F.; Bartlett, R. J. *J. Chem. Phys.* **1993**, *98*, 7029.

(39) Humphrey, W.; Dalke, A.; Schulten, K. *J. Mol. Graphics* **1996**, *14*, 33.

(40) Sobolewski, A. L.; Domcke, W. *Chem. Phys. Lett.* **1991**, *180*, 381.

(41) Oldani, M.; Bauder, A. *Chem. Phys. Lett.* **1984**, *108*, 7.

(42) Lombardi, J. R.; Wallenstein, R.; Hänsch, T. W.; Friedrich, D. M. *J. Chem. Phys.* **1976**, *65*, 2357.